Electronic transport across linear defects in graphene

C. J. Páez,[1,*] J. N. B. Rodrigues,[2] A. L. C. Pereira,[1] and N. M. R. Peres[3]

[1] *Faculdade de Ciências Aplicadas, Universidade Estadual de Campinas, 13484-350 Limeira, SP Brazil*
[2] *Centre for 2D Advanced Materials and Graphene Research Centre, Faculty of Science, National University of Singapore, 6 Science Drive 2, Singapore 117546*
[3] *Centro de Física e Departamento de Física, Universidade do Minho, P-4710-057, Braga, Portugal*

(Dated: April 7, 2015)

We investigate the low-energy electronic transport across grain boundaries in graphene ribbons and infinite flakes. Using the recursive Green's function method, we calculate the electronic transmission across different types of grain boundaries in graphene ribbons. We show results for the charge density distribution and the current flow along the ribbon. We study linear defects at various angles with the ribbon direction, as well as overlaps of two monolayer ribbon domains forming a bilayer region. For a class of extended defect lines with periodicity 3, an analytic approach is developed to study transport in infinite flakes. This class of extended grain boundaries is particularly interesting, since the K and K' Dirac points are superposed.

PACS numbers: 73.63.-b,81.05.ue

I. INTRODUCTION

The synthesis of graphene by chemical vapor deposition (CVD) on metal surfaces is the most widely used method for producing graphene sheets.[1–4] CVD graphene, as any other solid grown by CVD, is especially prone to the formation of grain boundaries (GBs) and extended defect lines, which hinder its electronic properties.[5–9]

Graphene is being proposed for a variety of new electronic devices.[10,11] However, the required high-quality electrical properties are affected by the formation of polycrystalline structures.[12–15] These structures are practically unavoidable by the growth methods known so far.[7,8] As such, the scattering problem of an electron off a grain boundary (GB) becomes a theoretical and an experimental relevant one.[16–20]

The sp^2 bonding structure of carbon atoms in graphene gives rise to extended topological defects that are typically composed of pentagonal, heptagonal, and octagonal rings of carbon atoms, together with distorted hexagons.[5–8] GBs are in general neither perfect straight lines nor periodic, intercepting each other at random angles. However, periodic straight GBs and defect lines can also be observed in graphene,[6] and more interestingly they can be controllably synthesized at precise locations and orientations,[13,21] lifting the prospects for the engineering of arrays of such defects that would allow us to manipulate the electronic valley degree-freedom in graphene.

GBs are known to strongly influence the properties of graphene, namely its chemical, mechanical, and electronic ones.[22–26] GBs are expected to present different degrees of transparency to electron transport, depending on their microscopic details and on the relative orientations of the grains separated by them.[16,18,19,25,27,28] In fact, measurements of electronic mobilities of different CVD samples, have shown that their electronic properties strongly depend on the details of the CVD-growth recipes.[1,2,4,7] Interestingly enough, and of direct relevance to our work, recent research has probed the electric properties of single GBs.[12,29,30]

In a revealing work, Yazyev *et al.*[25] have studied electronic scattering from a wide variety of periodic GBs. In that work, based on momentum conservation along the periodic grain boundary, the authors have shed light on whether low-energy electrons travelling from one grain to the other may feel a transport gap at the GB. Their conclusions were also quantitatively corroborated by first-principles quantum transport calculations (based on density functional theory and the non-equilibrium Green's function formalism).

Our approach to the scattering problem due to GB's follows two different routes. In the first route we use the recursive Green's functions method to numerically calculate the transmission through defect lines in graphene ribbons. We map charge density over each sublattice site and also the current density through the defects. Following the experiments,[12–14] we consider grain boundaries composed of extended linear defects of type 585 (pentagons and octagons) and 5757 (pentagons and heptagons). Our results for the resistance across a linear defect compare well to recent experimental results.[12] We also consider graphene ribbons with bilayer GBs: a spatial region where the grain boundary is composed by the superposition of two monolayer domains, as shown in Fig. 1. For this kind of overlapping bilayer boundary, previous results have already shown interesting conductance oscillations.[31] Here we show that the transmission through these superpositions is reduced in comparison to the transmission in the single-crystal domains. We also present a spatial map of the current and the charge distribution through these overlapped regions, which helps in the understanding of the transport properties of these systems.

In the second route, we will concentrate on a particular class of extended grain boundaries briefly addressed by Yazyev *et al.*, namely, those grain boundaries with

periodicities such that both Dirac points (at each side of the grain boundary) are mapped into the Γ point of the projected Brillouin zone. In such cases, there will be intervalley scattering of massless Dirac fermions at the grain boundary.

We have chosen to investigate zigzag aligned extended linear defect lines separating two grains with the same orientation (also referred to in the literature as degenerate, i. e., zero misorientation angle, grain boundaries). Several such defect lines were proposed in the context of ab-initio works both on graphene and on boron nitride: the t7t5 defect line[32] and the 7557 defect line[33] (see Fig. 8) are two such defect lines. As we will see ahead, this defect line allows for valley scattering to occur and can thus be regarded as a useful nanostructure for valleytronics circuits.

For this second type of problems, and in the context of graphene's single particle first neighbor tight-binding model, we will use the transfer matrix formalism[18] to analytically compute the transmittance of electrons across these grain boundaries. The boundary condition seen by the electrons at the grain boundary will be determined from its microscopic tight-binding model. In doing so, we will follow the methodology developed for the cases of the pentagon-only, zz(558), and zz(5757) defect lines.[18,19] We will see that the obtained boundary condition explicitly introduces intervalley scattering.

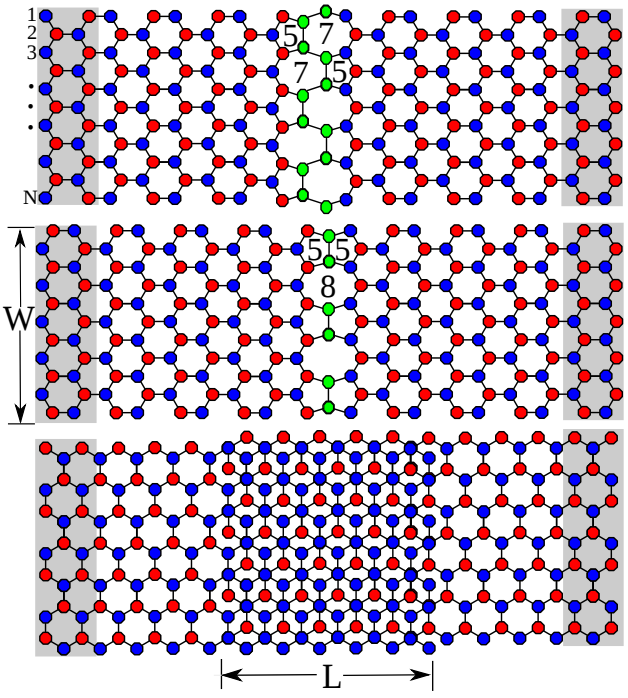

FIG. 1. (color online) Schematic representation of the different linear defect structures considered as grain boundaries. On the top is the 5757 structure. In the middle we show the 585 linear defect. At bottom is the bilayer graphene of length L, formed by the overlap of two monolayer regions. The shadow areas represent the left and right semi-infinite contacts.

II. TIGHT-BINDING MODEL AND TRANSPORT FORMALISM

We consider graphene's tight-binding Hamiltonian

$$H = -t_{i,j} \sum_{<i,j>} (c_i^\dagger c_j + \text{H.c.}) \tag{1}$$

where c_i ($c_i^\dagger$) annihilates (creates) an electron at site i and (i,j) stands for pairs of nearest-neighbor atoms. We use the value of $t_{i,j} = 2.7$ eV for the inplane nearest-neighbor hopping parameter and, when modeling the region of bilayer graphene, we use $t_{ij,\perp} = 0.381$ eV for the interlayer coupling.[34] The extended linear defects are constructed by rearranging the positions of the atoms in the defect region. As shown in Fig. 1, this modifies the topology of the lattice and thus changes pristine graphene's Hamiltonian in Eq. (1).

Coherent transport across grain boundaries in graphene is studied within the Landauer-Büttiker formalism, which relates the conductance $G(E)$ at a given energy E to the transmission function $T(E)$ between the contacts as

$$G(E) = G_0 T(E)\,, \tag{2}$$

with $G_0 = 2\frac{e^2}{h} \approx \frac{1}{12.5k\Omega}$. In the context of the previously referred first approach to scattering problems by GBs, the transmittance $T(E)$ is evaluated by means of the recursive Green's function approach using a two-terminal device configuration with contacts represented by the semi-infinite ideal graphene leads

$$T = Tr\left[\Gamma_L G_S^\dagger \Gamma_R G_S\right]\,, \tag{3}$$

where G_S is the retarded Green's function of the system, given by[35]

$$G_S = [E'I - H_S - \Sigma_L - \Sigma_R]^{-1}\,. \tag{4}$$

In these expressions H_S is the Hamiltonian for the scattering region, $\Sigma_{L(R)} = t^2 g_{L(R)}$ stand for the self-energies coupling the scattering region to the leads, while E' is a shorthand for $E' = E + i\eta$, with $\eta \to 0$. The self-energies and the broadening function $\Gamma_{L(R)} = i\left(\Sigma_{L(R)} - \Sigma_{L(R)}^\dagger\right)$[35] are calculated from the electrode's Green's function $g_{L(R)}$ also obtained numerically using a recursive technique.[36]

Charge and current are intimately related through the continuity equation. The connection with the Green's function arises from the quantum statistical average of the bond charge current operator, $\hat{J}_{ij} = \frac{e}{i\hbar}\left[t_{ji}c_j^\dagger c_i - t_{ij}c_i^\dagger c_j\right]$, which is related to the lesser Green's function $G_{ji}^<(E)$.[35,37] In a steady state the bond charge current

including spin degeneracy is:

$$J_{ij} = I_0 \int_{E_F^-}^{E_F^+} \mathrm{d}E \Big[t_{ji} G^<_{ij}(E) - t_{ij} G^<_{ji}(E) \Big] , \qquad (5)$$

where $E_F^{\pm} = E_F \pm eV/2$, while I_0 stands for the natural unit of bond charge current density being given by $I_0 = 2e/h \approx 77.5\,\mu$A/eV.

The lesser Green's function in the absence of interactions can be solved exactly giving $G^<(E) = G_S(E)[\Gamma_L f_L + \Gamma_R f_R] G_S^\dagger(E)$, where $f_{L(R)}$ is the Fermi distribution of the left (right) contact and t_{ji} is the hopping parameter between sites j and i. The bond current J_{ij} can be visualized as a bundle of flow lines bunched together along a link joining the two sites.

Complementary to the current density, the charge density at site j can also be expressed using the lesser Green's function as:

$$\rho_{(j)} = \frac{e}{2\pi i} \int_{E_F - eV/2}^{E_F + eV/2} dE G^<_{j,j}(E) . \qquad (6)$$

It is noteworthy that at low bias and low temperature the charge density ρ, has the same distribution of the local density of states (LDOS). Given that we are interested in how charge and current distributions are related, to keep explanations and figures as simple as possible, we will refer from now on to LDOS as charge distribution, with no loss of generality.

In addition to the Landauer-Buttiker formalism [see Eq. (2)], it has been shown[18,19] how can we compute the low-energy limit of the conductance across this kind of defect lines. Interestingly, at low temperatures, the conductance across a defect line of size W [see Fig. 1] turned out to be linear in $K_F W$ and proportional to the transmittance [see Eq. (3)] close to Dirac point ($E \to 0$):

$$G(E) = W \frac{g_v g_s}{4\pi} \left| \frac{E}{\hbar v_F} \right| G_0 T(E) . \qquad (7)$$

The gate voltage V_g is nothing more than the spatial potential distribution created by the substrate's charge distribution. We have estimated V_g for the GBs from the capacitor law

$$V_g = \frac{qnd}{\epsilon A} , \qquad (8)$$

where n stands for the carrier density, d is the thickness and ϵ is the dielectric constant of the substrate. In order to convert the experimentally measured gate voltage into carrier density n we use the relation $V_g = n/\alpha$, where $\alpha = 2.5 \times 10^{12}\ m^{-2}V^{-1}$ is a geometry-related factor. From here onward, we will only consider the carrier density to be $n = g_s g_v K_F^2/4\pi$, where K_F is the momentum at the Fermi energy and g_v (g_s) stands for the valley (spin) degeneracy. Finally, as in graphene E_F and K_F are proportional at low-energy, $E_F = \hbar v_F K_F$, then

$$V_g(E) = \tfrac{1}{\alpha} \tfrac{g_s g_v}{4\pi} (\tfrac{E}{\hbar v_F})^2 , \qquad (9)$$

From Eq. (7) and Eq. (9) one can expect that the resistance of a periodic defect line, at low temperatures and in the linear regime, should behave as

$$R = \frac{1}{G} \propto \frac{1}{\sqrt{V_g}} . \qquad (10)$$

This square root dependence on V_g should be clear from the experimental measurements of the resistivity across a grain boundary.

III. MODIFIED CONDUCTANCE QUANTIZATION IN THE PRESENCE OF THE LINEAR DEFECT

The study of scattering by extended defects is becoming increasingly more relevant, specially after the recent

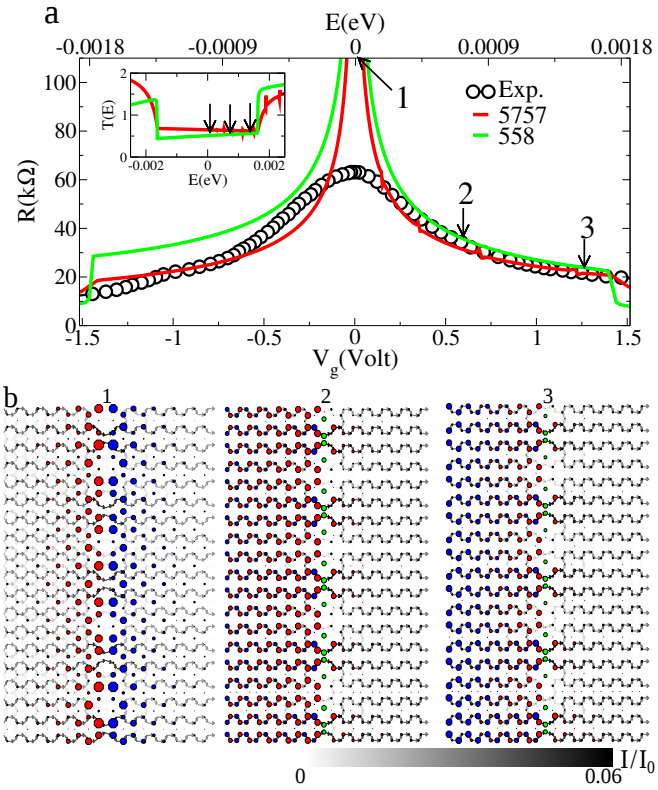

FIG. 2. (color online)(a) Resistivity across the grain boundaries structures 5757 and 585, compared to the experimental results of Tsen *et al.*[12]. Inset: Transmission function. Here we used an armchair ribbon with $g_s = 2$, $g_v = 1$, $N = 56$ atoms along the width and making further correspondence to $W = 1\mu$m. (b) Spatial distribution of charge densities and current densities over the GB for different energies: $E = 10^{-7}$ eV, $E = 7 \times 10^{-4}$ eV and $E = 14 \times 10^{-4}$ eV . The charge densities are schematically represented here for a narrower ribbon. The current densities are evaluated at different sites. The color of the arrow represents the magnitude of the electric current between any two neighboring sites, which are linearly normalized to the maximum value.

work by Tsen *et al.*,[12] where the authors made electric measurements across a single grain boundary. They have found that the transport properties of these systems are strongly dependent on the GB's microscopic details.

Using Eq. (7) and Eq. (10) we calculate the resistance across two linear defects, the 5757 and the 585, and compare them with the experimental result from Tsen *et al.* (black circles) – Fig. 2(a). We verify that they agree to a good extent for V_g not too close to the Dirac point. The disagreement (at low carrier densities) between the experiment and our prediction is due to the effect of puddles, which are not taken into account in our calculations, and dominate the bulk region of the device. Note that the effect of puddles is increasingly relevant when one approaches energies very close to the Dirac point. In order to obtain the above results, we have considered an armchair ribbon with $N = 8132$ sites ($g_s = 2$, $g_v = 1$ and $W \approx 1\mu$m). The electronic properties at low-energy regimes, are obtained by a rescaling of the electronic properties of an armchair ribbon with $N = 500$ sites.

The transport properties of these different linear defects are qualitatively similar. In the inset of Fig. 2(a) we show the electronic transmission and how it depends on the detailed geometry of the GB. In the continuum low-energy limit, both the 585 and the 5757 defects have a metallic behavior with a flat band crossing the Fermi level.

The spatial distribution of charge density (for different energies) of a 585 linear defect is shown in Fig. 2(b). The density on each atomic site is represented as a disk. The different colors (red and blue) identify the sublattice, while the magnitude of the disk's radius is proportional to the charge density at that site. We can see that the closer we are to the Dirac point ($E = 10^{-7}$eV) the more localized the charge is in the region of the GB. We also plot on Fig. 2(b) the distribution of charge density for higher energies. In this case, a higher dispersion of the charge is apparent mainly before the 585 structure: the line defect acts as a potential wall.

The corresponding current densities are also shown in Fig. 2(b), being evaluated at different sites using Eq. (5). The color of the arrow represents the magnitude of the electric current between any two neighboring sites, which are linearly normalized to the maximum value, according to the greyscale bar. For all the plotted energies, we observe that before and after the linear defect, the current flows in a specific horizontal pattern along armchair paths (streamlines) skipping some horizontal bonds, in accordance with recent ab-initio calculations of the current densities in pristine armchair graphene ribbons.[38] Here, with the linear defect, it is interesting to observe how the current gives priority to some paths within the defect line, also in a periodical pattern. One can also see that the current density is smaller for the first represented energy (i. e., $E = 10^{-7}$ eV), as would be expected due to the localized nature of the charge density around the defect for this energy.

IV. LINEAR DEFECT ORIENTATION

The transmission across linear defects is known to significantly depend on their orientation angle.[19,39,40] In Fig. 3(a)-(d), we show schematic representations of four different orientations of a 585 extended defect in a graphene ribbon: $\theta = 0°, 30°, 60°$ and $90°$. In Fig. 3(e) we plot the transmission probability as a function of the energy for these different angles of incidence at the defect. For all cases, we see that the particle-hole symmetry is broken due to the translation symmetry breaking introduced by the defect.

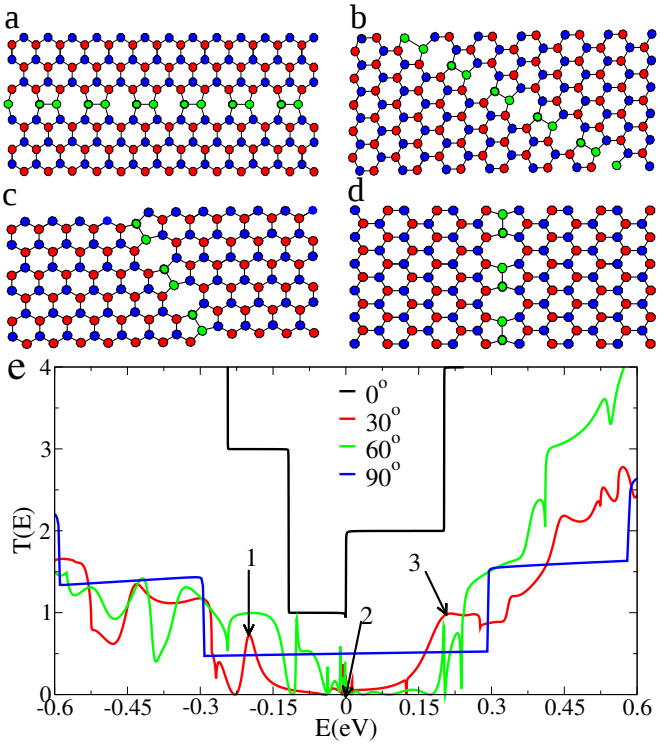

FIG. 3. (color online) Schematic representation of a linear defect 585 at different orientation angles (a) 0°, (b) 30°, (c) 60° and (d) 90°. (e) Transmission probability for each angle. The ribbon has $N = 56$ sites in the width.

For $\theta = 0°$, the presence of the defect line located in the middle of the ribbon does not alter the metallic character observed in the transmission spectrum of a pristine armchair ribbon of the same width.[41] Fig. 3(e) also shows that for $\theta = 30°$ and 60° there are regions of vanishing transmission (opening of transport gap) close to the Dirac point. To further investigate the origins of these oscillations in the transmission, in Fig. 4 we map the charge and current density distributions for the selected energies indicated (by the arrows 1, 2 and 3) in Fig. 3(e).

The first energy (arrow 1) corresponds to a transmission resonance at an energy $E = -0.21$ eV, which is typical of resonant tunneling structures, where the con-

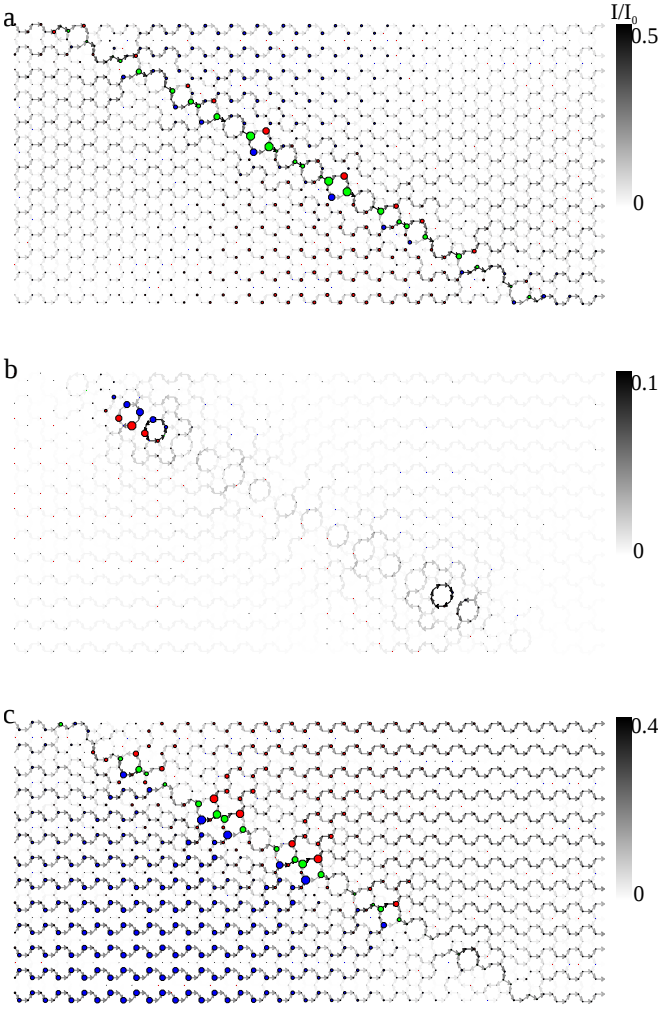

FIG. 4. (color online) Spatial distribution of charge densities and current densities over the linear defect 585 with a orientation angle of $\theta = 30°$, to corresponding to the energies indicated by the numbered arrows in Fig. 3(b): $E = -0.21$ eV, $E = 1 \times 10^{-7}$ eV and $E = 0.21$ eV.

tinuum background is strongly suppressed at the discrete state localization. The associated charge and current density distribution are shown in Fig. 4(a). A high current density exactly following the defect line reveals its metallic character. Close to the contacts and far from the defect line, the current flow splits again into streamlines.[38] A similar behavior (high current density located along the linear defect) is found for resonances at angle of 60° (not shown here). We also found that the resonances of the first channel in the angles 30° and 60° are robust structures independent from W. The present results suggest an image of Fano-type resonances, a finite coupling between the localized state associated to the linear defect and the delocalized continuum states associated with the armchair ribbon.

In Fig. 4(b), we show the charge and current density distribution for the second selected energy [arrow 2 in Fig. 3(e)], corresponding to a vanishing transmission close to the Dirac point. Interference in charge and current density on both sides of the linear defect can be seen, as well as on the linear defect. For this low energy we observe that the charge distribution is highly localized in part of the defect. The current seems not to flow, with its maximum local values circulating around the octagons where the charge is concentrated and around octagons symmetrically positioned with respect to the middle of the linear defect. Note that the directions of the small arrows representing the local current flow around the octagons is different for Fig. 4(b) (local loopings) and Fig. 4(a) (net flow). The backscattering is evident. Therefore we conclude that at low-energies, i. e., close to Dirac point, the suppression of the transmission, at the first electron-like plateau, is due to charge localization and backscattering of a defect-related mode of the 585 defect line.

Fig. 4(c) corresponds to an energy value of $E = 0.21$ eV. One can see that the current throughout the ribbon is not uniform and forms ambiguous paths. At this energy, the current-density amplitude also flows across the defect, being greater in the edge region than in the center of the ribbon. The flow is mostly perpendicular to the linear defect. Note that an electron can travel between the source and the drain via many different transport channels. The local electric current profile at a given energy is nothing more than the result from the interference between all the active transport channels at that energy. In particular, the existence of current loops for some defect orientations (see panels of Fig. 4), simply results from particular interference patterns arising from the different blockade of distinct transport channels by the linear defect. Moreover, the particular local current patterns that are observed result from the interplay between the different components of the nanostructure: linear defect topology and orientation, edges type and width of the graphene ribbon. In Fig. 3(b), for $\theta = 90°$, the first plateau does not present interference oscillations, the transmission is reduced in the vicinity of the Dirac point, due to the coupling of extended states at the edges with localized ones at the defect line. The oscillations at high energy range are simply Fabry-Perot interference effects.

V. BILAYER GRAPHENE AS A GRAIN BOUNDARY

In this section we investigate the electronic transport properties of a grain boundary defined by an overlap between two semi-infinite monolayer graphene regions, forming a bilayer region as represented in Fig. 5(a). Such overlaps have been experimentally observed.[12] Here, to focus on the effects of the bilayer region on the transmission, we consider periodical boundary conditions, avoiding edge localization effects.

Figure 5(b) and (c) shows the transmission T(E) as a function of energy across a bilayer region of length L cor-

responding to 80 and 320 atoms superposed, respectively. We consider both the AB (Bernal) and AA stacking cases for the overlap regions. For both of them oscillations in the transmission are observed, with their frequency increasing for increasing overlap length L, in agreement with previous calculations for similar overlaps.[31] This can be qualitatively understood by remembering that in such systems, the transmittance is set by the wave-function matching at the monolayer-bilayer interfaces. A monolayer eigenstate incoming from the left is going to be partially transmitted into the bilayer region and partially reflected back into the left monolayer. The portion of the wave-function transmitted into the bilayer region is going to propagate (acquiring a complex phase) until the second interface (bilayer-monolayer) and there it will undergo a similar scattering process: it is going to be partially reflected back to the bilayer and partially transmitted into the right monolayer. The resultant standing wave, in particular, the weight associated with each of its components (channels), is going to be the direct result of this interference process and will thus strongly depend on the length of the bilayer region and on the wave-number associated with each of those channels. The phases acquired by each of the wave-function's components of the bilayer region at the second interface are going to be smaller for shorter bilayer regions (i. e., shorter L). In such cases, oscillations in the transmittance will require a greater change of the eigenstates' wave-number, i. e., a greater increase in energy, as observed in both panels of Fig. 5. For comparison, we also show in Fig. 5(b) and (c) the transmission through a pristine monolayer and pristine bilayers AA and AB (considering the same width, 40 atoms, to which periodic boundary conditions are applied). One can see that the transmission through the pristine monolayer and bilayers is always higher than the transmission throughout the overlapped region. This is due to the presence of the interfaces, that act as scattering centers decreasing the system's transmission. Figure 5(d) shows the band structure for pristine monolayer and pristine bilayers AA and AB (of same width and also with periodical boundary conditions), which helps in understanding the origin of the plateaus in the transmission for each case. At low energies, in the case of AB stacking there is only one conducting channel, whereas in AA stacking there are always two conducting channels for each valley. This partially explains why in general the low-energy transmission for the AB bilayer structure is smaller than that for the AA bilayer structure. But in addition to this, we can easily check that the boundary condition at a monolayer-bilayer AA interface can be completely satisfied at low energies without the need for reflected components in the monolayer region. The same does not happen for the case of the monolayer-bilayer AB interface. Therefore, the upper bound for the transmission at low energies is smaller in the bilayer AB case than in the bilayer AA case. Nevertheless, and by appropriately choosing the bilayer region length, L, we can still make bilayer AB case's low-energy transmission higher than that of the bilayer AA case.

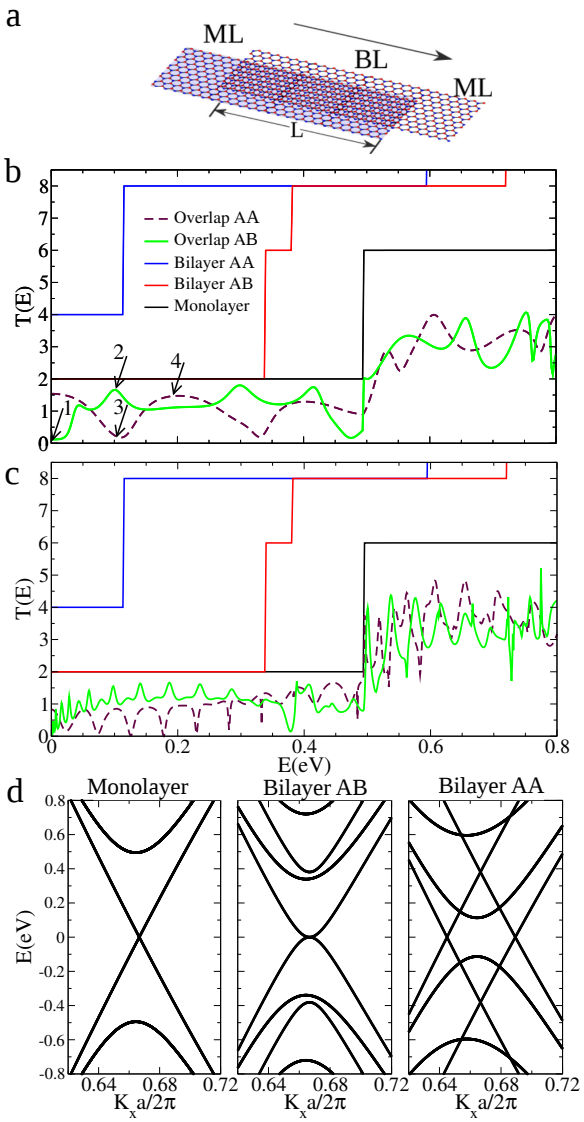

FIG. 5. (color online) (a) Schematic representation of the overlap between two graphene monolayers, forming a bilayer region of length L. (b) Transmission throughout a bilayer region of length L corresponding to 80 atoms superposed. Both AA and AB stackings are considered for the overlap (bilayer region). For comparison, it is shown the transmission through a pristine monolayer and pristine bilayers AA and AB of same width. (c) Same as in (b), showing now the transmission throughout a bilayer region of length L corresponding to 320 atoms superposed. (d) Band structures for pristine monolayer and pristine bilayers AA and AB of same width.

In Fig. 6 we map the spatial distribution of charge density and local current density on each of the overlapping (AB stacking) graphene monolayer ribbons. Figure 6 (a) and (b) show such maps corresponding to the energies $E = 0.001$ eV and $E = 0.1$ eV, indicated by arrows 1 and 2 in Fig. 5, respectively a minimum and a maxi-

mum values of transmission in the low-energy limit. For $E = 0.001$ eV, i. e. in Fig. 6(a), the charge density is localized mainly on the left semi-infinite monolayer, which corresponds to the bottom layer in the bilayer region. On right semi-infinite monolayer (i. e., the top layer of the bilayer region), the charge density rapidly decreases from the left to the right. In particular, its charge density is insignificant in the monolayer region. In the regions with non-vanishing charge density of each layer, the charge density typically concentrates on only one sublattice: the non-dimer sublattice. This effect comes from the sublattice asymmetry introduced by the AB-stacking in bilayer graphene.[42,43] Moreover, for this energy, the current density is very low on both layers. On the other hand, for $E = 0.1$ eV (which corresponds to a peak in the transmission), we can see in Fig. 6(b) that again the charge seems to be polarized on the non-dimer sublattice in the central part of the bilayer region. However, a careful observation of other parts of the bilayer region shows that the charge is more homogeneously distributed over both sublattices there, thus allowing electron hopping between sites and between layers,[44,45] as observed in the pattern of the zigzag current density streamlines.

Similarly, in Fig. 7 we show the charge and current density distribution for the case of the two monolayers with an AA-stacking overlap region. Figure 7(a) corresponds to $E = 0.11$ eV (the minimum in transmission indicated by the arrow 3 in Fig. 5), while Fig. 7(b) corresponds to $E = 0.2$ eV (the resonance in transmission indicated by the arrow 4 in Fig. 5). For both energies, there is a clear charge wave along the bilayer length with charge oscillating between the two layers. Similarly, current also oscillates between layers. However comparing charge and current densities in each layer, one can see an interesting behavior: for the energy corresponding to low transmission, Fig. 7(a) shows that there is a clear imbalance, since the electronic charge density and the current density are concentrated on different parts of the bilayer region. On the other hand, in Fig. 7(b), i. e., for the energy corresponding to high transmission, we again observe a charge and current oscillation between layers along the length of the bilayer region, but now these are in phase, with the maximum current density spatially coinciding with the maximum charge density. Also note the higher current densities associated with the later energy (see different current grey scale bar).

VI. TRANSPORT ACROSS THREE PERIODIC GRAIN BOUNDARIES: TRANSFER MATRIX APPROACH

In this section we use the transfer matrix formalism[18] to study the electronic transport across extended grain boundaries in the scope of the single particle first neighbor tight-binding model of (infinite) monolayer graphene. This method is entirely equivalent to the recursive Green's function numerical method used up to this point of the manuscript. It reduces the electronic scattering problem to a set of matrix manipulations easy to work out by any computational algebraic calculator, and thus give rise to an analytic solution of the problem.

We will concentrate on a particular class of zigzag aligned periodic GBs that separate grains with the same orientation (also known as zero misorientation angle GBs) and have a periodicity that allows for intervalley scattering of low-energy electrons. When the periodicity of the zigzag aligned GBs is a multiple of 3, both Dirac points (as well as the Γ-point) are mapped into $k_x a = 0$ – see panels (c) and (d) of Fig. 9. Therefore, and in contrast with what happens for the pentagon-only, 585 and 5757 GBs,[16,18,19,27,28] linear momentum conservation does not forbid low-energy electrons from scattering between valleys. Nevertheless, and if we want to know how much intervalley scattering is a particular GB going to generate, we need to explicitly compute the boundary condition matrix originating from its tight-binding microscopic model.

From the diversity of GBs belonging to this class, we have chosen to investigate some that have been recently suggested in the context of ab-initio works both on graphene and on boron nitride: the 7557 grain boundary[33] and the t7t5 grain boundary[32] (see Fig. 8). As we will see ahead, these GBs controllably scatter electrons from one valley to the other and can thus be regarded as a useful nanostructure for valleytronics circuits, whenever the desire is to destroy valley polarization.

A periodic GB preserves the crystal's translation invariance along the GB direction. Therefore, by Fourier transforming the system's tight-binding Hamiltonian along this direction, we can cast the problem of electronic transport in a 2D crystal with a GB at its center, as a problem of electronic transport on a quasi-1D crystal with a localized defect at its center.

In order to work out this problem we will proceed as in Ref. 18. From pristine graphene's Hamiltonian we start by writing the tight-binding equations away from the grain boundary (see Figs. 12 and 13 for notation clarification)

$$-\frac{\epsilon}{t}\mathbf{A}(n) = W_A^\dagger \mathbf{B}(n-1) + \mathbf{B}(n), \tag{11a}$$

$$-\frac{\epsilon}{t}\mathbf{B}(n) = \mathbf{A}(n) + W_A \mathbf{A}(n+1), \tag{11b}$$

where we have used the notation $\mathbf{Z}(n) = [Z_1(n), Z_2(n), Z_3(n)]^T$ for $Z = A, B$ (sub-lattice identifier). Note that the notation is hiding the dependency of the A_i and B_i on k_x, the momentum along the grain boundary direction. In the above expressions, ϵ and t stand respectively for the energy and pristine graphene's hopping parameter, while n gives the number of direct lattice vector $\mathbf{u}_2 = (-1, \sqrt{3})a/2$ translations away from the defect (see Figs. 12 and 13). The matrix

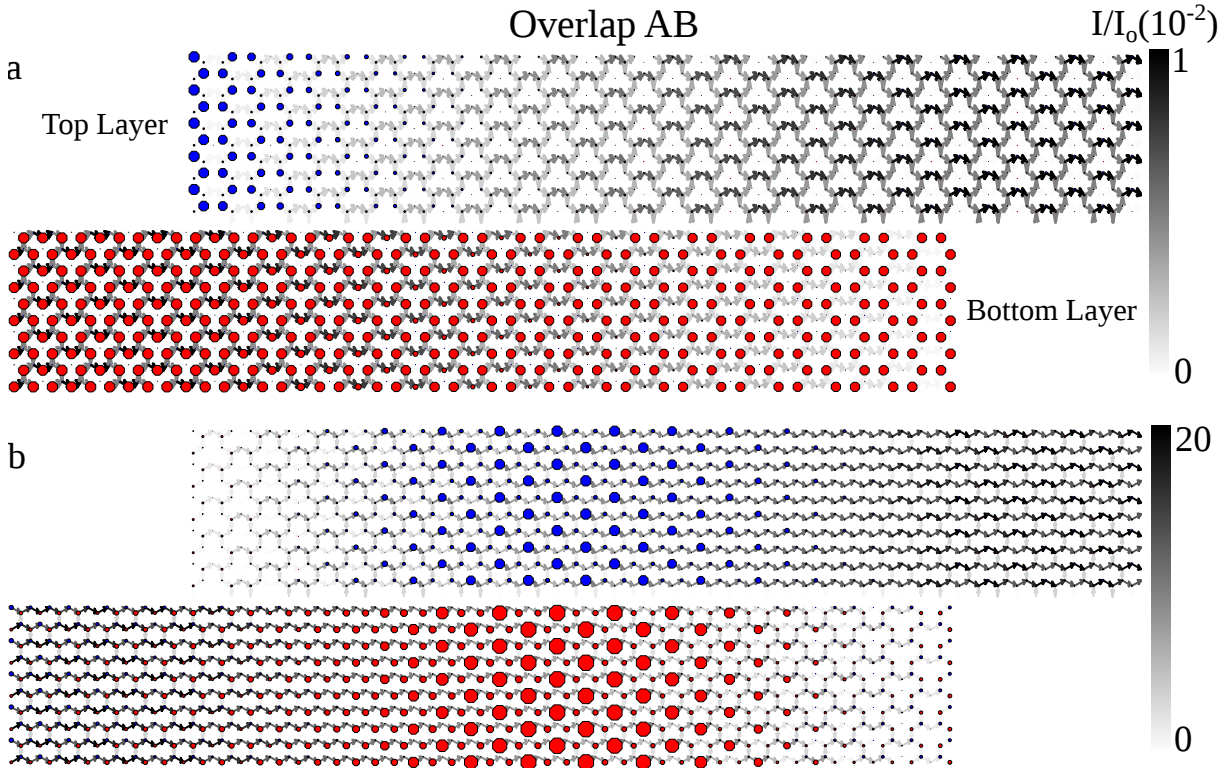

FIG. 6. (color online) Charge and current density distributions for the nanostructure composed of two graphene (monolayer) ribbons that partially overlapped (AB-stacked in the overlap/bilayer region). The two panels stand for two different energies: (a) $E = 0.001$ eV, which corresponds to a minimum of transmission (indicated by the arrow 1 in Fig. 5). (b) $E = 0.1$ eV, which corresponds to a maximum of transmission (indicated by the arrow 2 in Fig. 5).

W_A reads

$$W_A = \begin{bmatrix} 1 & 1 & 0 \\ 0 & 1 & 1 \\ e^{3ik_x a} & 0 & 1 \end{bmatrix}. \tag{12}$$

We can write the above tight-binding equations in the form

$$\begin{bmatrix} \mathbf{B}(n) \\ \mathbf{A}(n) \end{bmatrix} = \mathbb{Q}_1 \begin{bmatrix} \mathbf{A}(n) \\ \mathbf{B}(n-1) \end{bmatrix}, \tag{13a}$$

$$\begin{bmatrix} \mathbf{A}(n) \\ \mathbf{B}(n-1) \end{bmatrix} = \mathbb{Q}_2 \begin{bmatrix} \mathbf{B}(n-1) \\ \mathbf{A}(n-1) \end{bmatrix}, \tag{13b}$$

where the matrices $\mathbb{Q}_1$ and $\mathbb{Q}_2$ read

$$\mathbb{Q}_1 = -\begin{bmatrix} \frac{\epsilon}{t}\mathbb{I}_3 & W_A^\dagger \\ -\mathbb{I}_3 & 0 \end{bmatrix}, \tag{14a}$$

$$\mathbb{Q}_2 = -\begin{bmatrix} \frac{\epsilon}{t}(W_A)^{-1} & (W_A)^{-1} \\ -\mathbb{I}_3 & 0 \end{bmatrix}, \tag{14b}$$

with $\mathbb{I}_3$ standing for the 3×3 unit matrix.

Eqs. (13) can be written in the form of a transfer matrix equation[18,19] relating amplitudes at the atoms of the unit cell located at $(n-1)\mathbf{u}_2$ with the amplitudes at the atoms of the unit cell located at $n\mathbf{u}_2$. Such an equation reads

$$\mathbf{L}(n) = \mathbb{T}(\epsilon, k_x)\mathbf{L}(n-1), \tag{15}$$

with $\mathbf{L}(n) = [A_1(n), B_1(n), A_2(n), B_2(n), A_3(n), B_3(n)]^T$, and the transfer matrix, $\mathbb{T}(\epsilon, k_x)$, given by

$$\mathbb{T}(\epsilon, k_x) = R.\mathbb{Q}_1.\mathbb{Q}_2.R^T. \tag{16}$$

In the above equation, matrix R is simply used to change from the basis $\{B_1, B_2, B_3, A_1, A_2, A_3\}$ to the basis $\{A_1, B_1, A_2, B_2, A_3, B_3\}$. It is written in Eq. (A1).

Following the method used for the cases of the 585 and 5757 defect lines,[18,19] we can find a basis where the transfer matrix becomes block diagonal with three 2×2 matrices on its diagonal. In this basis the three modes of the problem are uncoupled. Moreover, around $k_x = 0$ two of these modes are low-energy (corresponding to each of the two Dirac cones), while the other is a high-energy mode.

We can understand this fact from Fig. 9(b) where one represents the First Brillouin zone (FBZ) originating from a honeycomb lattice whose direct vectors are chosen to be $3\mathbf{u}_1$ and $\mathbf{u}_2$. In such a FBZ, the two Dirac points are located at the same value of k_x, i. e., at $k_x = 0$. It is thus natural that when setting $k_x = 0$ in the transfer matrix given by Eq. (16), one obtains a transfer matrix that describes simultaneously low-energy electrons at each of the two valleys (together with an additional high-energy mode associated with the Γ-point region of the spectrum of pristine graphene).

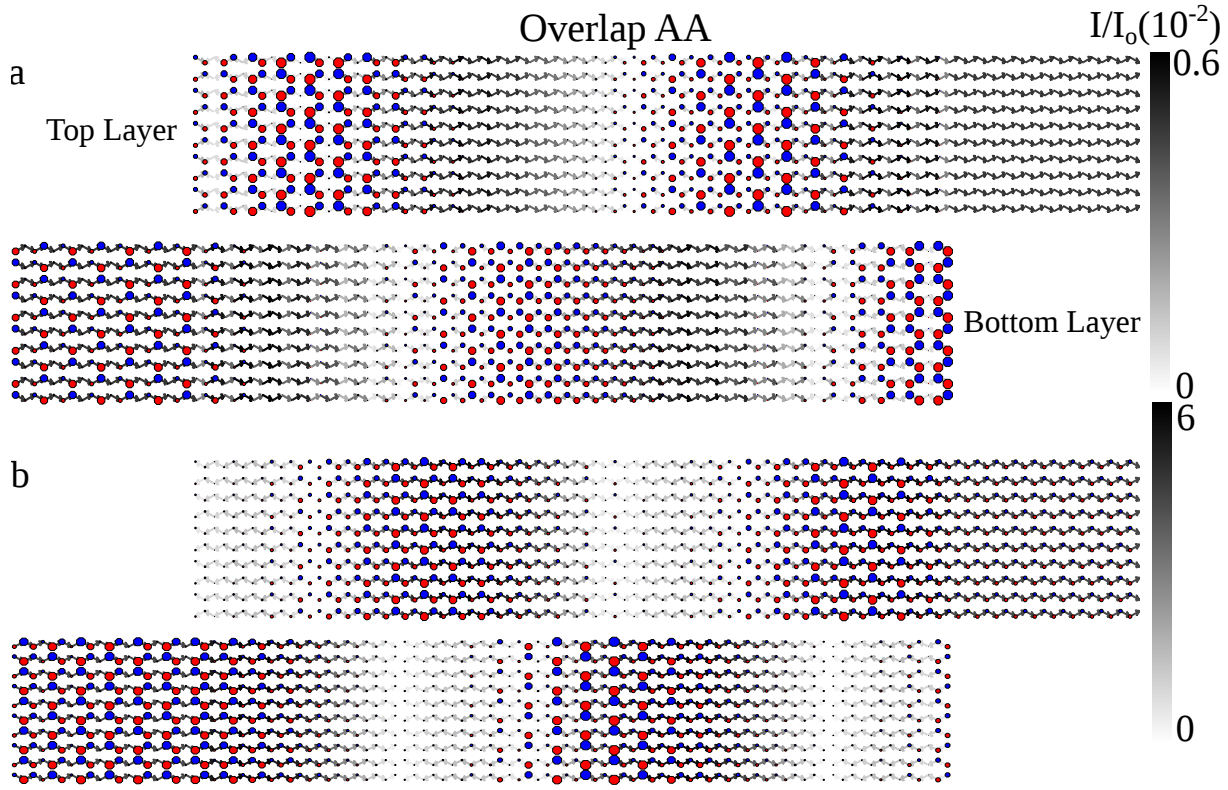

FIG. 7. (color online) Charge and current density distributions for the nanostructure composed of two graphene (monolayer) ribbons that partially overlapped (AA-stacked in the overlap/bilayer region). The two panels stand for two different energies: (a) $E = 0.11$ eV, which corresponds to a low transmission (indicated by the arrow 3 in Fig. 5). (b) $E = 0.2$ eV, which corresponds to a maximum of transmission (indicated by the arrow 4 in Fig. 5).

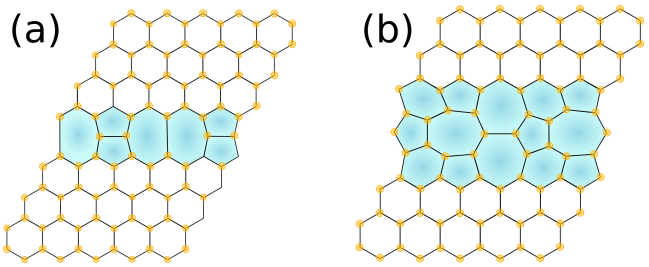

FIG. 8. Scheme of two grain boundaries proposed in the context of ab-initio works both on graphene and on boron nitride. (a) the 7557 defect line[33] and (b) the t7t5 defect line.[32] In these schemes we highlight in blue the region of the grain boundary.

The symbol $\Lambda(k_x)$ stands for the matrix mediating the change to the basis uncoupling the modes of the transfer matrix

$$\widetilde{\mathbf{L}}(n) = \Lambda(k_x)\mathbf{L}(n). \tag{17}$$

We will denote the states in this new basis as

$$\widetilde{\mathbf{L}} = [A_h, B_h, A_{l-}, B_{l-}, A_{l+}, B_{l+}], \tag{18}$$

with h identifying the mode with high-energy when $k_x \approx 0$, while $l+$ and $l-$ stand for the two modes with low-energy when $k_x \approx 0$, one associated with the $\mathbf{K}_-$ valley and the other with the $\mathbf{K}_+$ valley. The matrix $\Lambda(k_x)$ is explicitly written in Eq. (A2).

As previously stated, in this basis the transfer matrix, $\widetilde{\mathbb{T}}(\epsilon, k_x)$, is block diagonal and reads

$$\widetilde{\mathbb{T}}(\epsilon, k_x) = \begin{bmatrix} \mathbb{T}_h(\epsilon, k_x) & 0 & 0 \\ 0 & \mathbb{T}_{l-}(\epsilon, k_x) & 0 \\ 0 & 0 & \mathbb{T}_{l+}(\epsilon, k_x) \end{bmatrix}, \tag{19}$$

where the three transfer matrices associated with each of the uncoupled modes are written in Eqs. (A3).

A. The transmittance across the 7557 and the t7t5 grain boundaries

In a similar manner, the tight-binding Hamiltonian describing the electronic structure close to the grain boundary can be used to write the tight-binding equations for the defect. With these we can compute a boundary condition relating amplitudes on either side of the defect

$$\mathbf{L}(1) = \mathbb{M}.\mathbf{L}(-1), \tag{20}$$

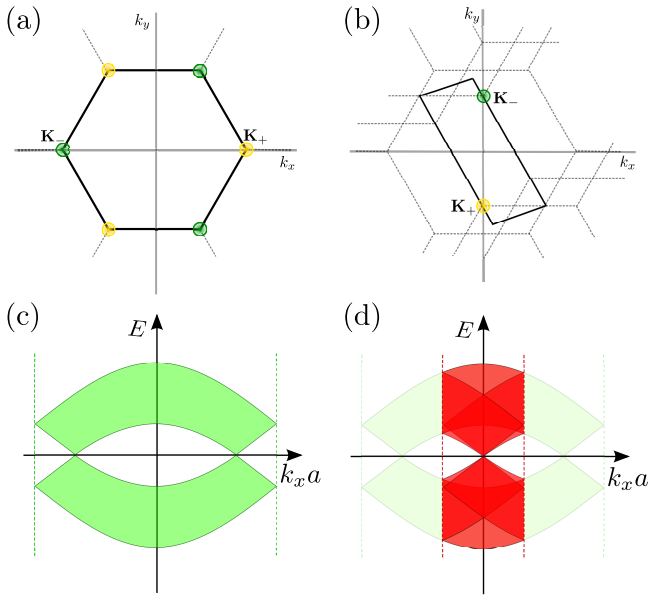

FIG. 9. (a) FBZ of pristine graphene (whose direct lattice vectors can be chosen to be $\mathbf{u}_1 = a(1,0)$ and $\mathbf{u}_2 = a(-1,\sqrt{3})/2$). (b) FBZ of graphene whose unit cell has thrice the size of that of pristine graphene in the zigzag direction (direction of $\mathbf{u}_1$). In this case, the direct lattice vectors can be chosen to be $3\mathbf{u}_1$ and $\mathbf{u}_2$ (as done in Figs. 12-13). (c) Spectrum of pristine graphene projected along the k_x direction (parallel to the GB). (d) Comparison between the k_x-projected spectrum of (unfolded) pristine graphene (light green) and the same spectrum after a triple folding (red): in the latter, the two valleys (and the Γ-point) are mapped into $k_x a = 0$.

where the boundary condition matrix, $\mathbb{M}$, is a 6×6 matrix that depends both on the energy ϵ, x-momentum k_x and the electron hoppings characteristic of the grain boundary. In Appendix B we compute these matrices for the two grain boundaries we are investigating: the 7557 and the t7t5 grain boundaries (see Figs. 12 and 13).

Note that by expressing this boundary condition matrix in the basis that uncouples the modes of the transfer matrix $\mathbb{T}(\epsilon, k_x)$

$$\widetilde{\mathbb{M}} = \Lambda(k_x a).\mathbb{M}.[\Lambda(k_x a)]^{-1}\,, \tag{21}$$

we can conclude that in general, it mixes all the three modes of matrix $\mathbb{T}(\epsilon, k_x)$.

Given this, we now have all the ingredients needed to compute the coefficients involved in the electronic scattering by such defects. An incoming electronic wave from $n = -\infty$, will be scattered by the defect at $n = 0$ producing a reflected and a transmitted component. The wavefunction on each side of the defect will then be given by

$$\widetilde{\mathbf{L}}(n<0) = \lambda_{i>}^{n+1}\,\mathbf{\Psi}_i^{>} + \sum_{j=1}^{r_<} \rho_{ij}\,\lambda_{j<}^{n+1}\,\mathbf{\Psi}_j^{<}\,, \tag{22a}$$

$$\widetilde{\mathbf{L}}(n>0) = \sum_{j=1}^{r_>} \tau_{ij}\,\lambda_{j>}^{n-1}\,\mathbf{\Psi}_j^{>}\,, \tag{22b}$$

where ρ_{ij} and τ_{ij} are, respectively, the reflection and transmission scattering amplitudes from an incoming (from $n=-\infty$) state, $\mathbf{\Psi}_i^{>}$, into reflected, $\mathbf{\Psi}_j^{<}$, and transmitted, $\mathbf{\Psi}_j^{>}$, outgoing states. Finally, by imposing the corresponding boundary condition [see Eqs. (20) and (21)], we can compute the coefficients ρ_{ij} and τ_{ij} for a given energy and a given longitudinal momentum.

For both the t7t5 and the 7557 grain boundary we have set the hopping parameters in the region of the grain boundary by estimating the corresponding carbon-carbon distances originating from the ab-initio results of Refs. 32 and 33, and then using the parametrization[46]

$$\tau(r_{ij}) = \left(\frac{r_{ij}}{a_0}\right)^{-\alpha_2} \exp[-\alpha_3 \times (r_{ij}^{\alpha_4} - a_0^{\alpha_4})], \tag{23}$$

where r_{ij} stands for the distance between the carbons labeled by i and j (given in units of angstroms), the adimensional parameters $\alpha_2 = 1.2785$, $\alpha_3 = 0.1383$, $\alpha_4 = 3.4490$, while a_0 is the carbon-carbon distance in pristine graphene (in units of angstroms).

In Fig. 10 we present the transmission probability for the 7557 grain boundary (see scheme of Fig. 12 and Appendix B 1) of an incoming electron of the $\mathbf{K}_+$ valley. The several transmittance curves of this figure correspond to different energies and were drawn using the following hopping parameters at the defect: $\xi = 0.98$, $\gamma = 0.94$ and $\beta = 0.1$. One can see on the several panels of this figure that the intervalley scattering is comparable to the *valley-preserving* scattering. Both of them strongly depend on the energy and incidence angle, mainly due to the dependence on energy and k_x of the boundary condition matrix (see its computation in Appendix B 1).

Similar plots are presented in Fig. 11 for the t7t5 grain boundary (see scheme of Fig. 13 and Appendix B 2). These were obtained with the following hopping parameters: $\xi_1 = 1.06$, $\xi_2 = 0.95$, $\xi_3 = 0.83$, $\xi_4 = 0.80$, $\xi_5 = 1.30$, $\xi_6 = 1.05$, $\gamma_1 = 1.23$, $\gamma_2 = 1.20$, $\gamma_3 = 1.18$ and $\gamma_1 = 1.36$. In general, this choice of hopping parameters gives rise to a lower intervalley scattering at low energies than what is obtained for the 7557 grain boundary.

We finalize by noting that the above transmittance curves are strongly dependent on the choice of the hopping parameters. In particular, at low energies these are the only parameters determining the boundary condition matrix and therefore controlling the system's transparency to incident electrons. Moreover, the GB's scattering profile can be strongly enhanced or suppressed by small changes of the GB's hopping parameters. Therefore, we may expect that intervalley scattering at the GB is deeply sensitive to modifications of the lattice's geometry (namely strain) in the vicinity of the GB.

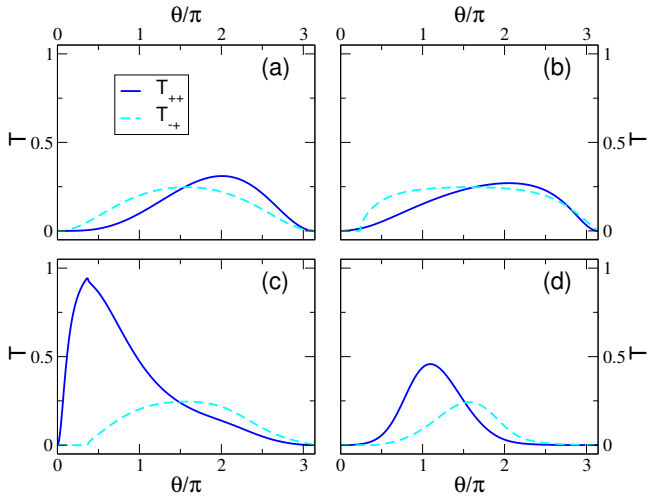

FIG. 10. Transmittance in terms of the incidence angle (incoming electron chosen to be on the valley $\mathbf{K}_+$ Dirac point) for the 7557 grain boundary. The panels (a), (b), (c) and (d) correspond to scattering processes occurring at energies of, respectively, $0.01t$, $0.1t$, $0.3t$ and $0.5t$. The hopping parameters (see Fig. 12) were set at: $\xi = 0.98$, $\gamma = 0.94$ and $\beta = 0.1$. The dark blue curve stands for the transmittance preserving the valley degree of freedom (electron from the $\mathbf{K}_+$ below the GB scattering scatters to the same valley above the GB, i. e. $T_{++} = |\tau_{++}|^2$). The dashed light blue curve stands for the intervalley transmittance (electron at the $\mathbf{K}_+$ valley below the GB scattering into the valley $\mathbf{K}_-$ above the GB, i. e. $T_{-+} = (v_-/v_+)\,|\tau_{-+}|^2$; $v_\pm$ stands for the velocity of the mode $l\pm$).

ACKNOWLEDGMENTS

NMRP acknowledges support from EC under Graphene Flagship (Contract No. CNECT-ICT-604391) and the hospitality of the Instituto de Física of the UFRJ, where this work was completed. JNBR acknowledges Singapore National Research Foundation for its support through the Fellowship Program NRF-NRFF2012-01. CJP and ALCP acknowledge So Paulo Research Foundation (FAPESP), grant 2012/19060-0. Part of the numerical simulations were performed at the computational facilities from CENAPAD-SP, at Campinas State University.

Appendix A: The bulk tight-binding equations

The matrix R changing from the basis $\{B_1(n), B_2(n), B_3(n), A_1(n), A_2(n), A_3(n)\}$ into the basis $\{A_1(n), B_1(n), A_2(n), B_2(n), A_3(n), B_3(n)\}$ reads

$$R = \begin{bmatrix} 0 & 0 & 0 & 1 & 0 & 0 \\ 1 & 0 & 0 & 0 & 0 & 0 \\ 0 & 0 & 0 & 0 & 1 & 0 \\ 0 & 1 & 0 & 0 & 0 & 0 \\ 0 & 0 & 0 & 0 & 0 & 1 \\ 0 & 0 & 1 & 0 & 0 & 0 \end{bmatrix}. \tag{A1}$$

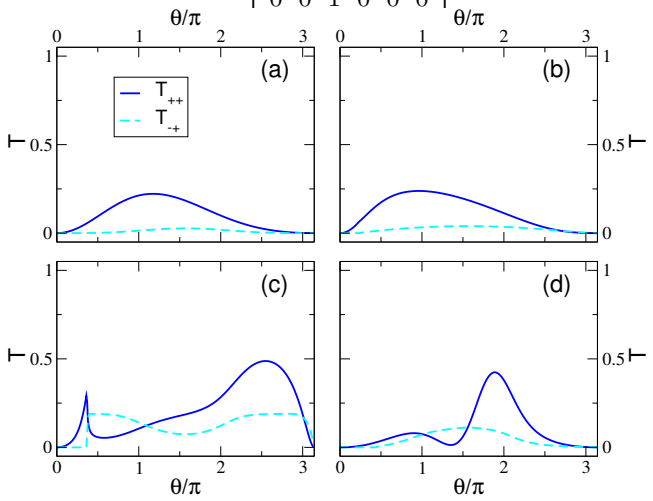

FIG. 11. Transmittance in terms of the incidence angle (incoming electron chosen to be on the valley $\mathbf{K}_+$ Dirac point) for the t7t5 grain boundary. The panels (a), (b), (c) and (d) correspond to scattering processes occurring at energies of, respectively, $0.01t$, $0.1t$, $0.3t$ and $0.5t$. The hopping parameters (see Fig. 13) were set at: $\xi_1 = 1.06$, $\xi_2 = 0.95$, $\xi_3 = 0.83$, $\xi_4 = 0.80$, $\xi_5 = 1.30$, $\xi_6 = 1.05$, $\gamma_1 = 1.23$, $\gamma_2 = 1.20$, $\gamma_3 = 1.18$ and $\gamma_1 = 1.36$. The dark blue curve stands for the transmittance preserving the valley degree of freedom (electron from the $\mathbf{K}_+$ below the GB scattering scatters to the same valley above the GB, i. e. $T_{++} = |\tau_{++}|^2$). The dashed light blue curve stands for the intervalley transmittance (electron at the $\mathbf{K}_+$ valley below the GB scattering into the valley $\mathbf{K}_-$ above the GB, i. e. $T_{-+} = (v_-/v_+)\,|\tau_{-+}|^2$; $v_\pm$ stands for the velocity of the mode $l\pm$).

The matrix mediating the basis change that uncouples the modes of the transfer matrix, $\Lambda(k_x)$, reads

$$\Lambda\left(\frac{\phi}{a}\right) = \frac{1}{\sqrt{3}} \begin{bmatrix} 1 & 0 & -\frac{e^{-i(\phi-2\pi/3)}i\sqrt{3}}{1+e^{i\pi/3}} & 0 & \frac{e^{-i2(\phi-2\pi/3)}i\sqrt{3}}{1+e^{-i\pi/3}} & 0 \\ 0 & 1 & 0 & -\frac{e^{-i(\phi-2\pi/3)}i\sqrt{3}}{1+e^{i\pi/3}} & 0 & \frac{e^{-i2(\phi-2\pi/3)}i\sqrt{3}}{1+e^{-i\pi/3}} \\ 1 & 0 & -e^{-i(\phi-\pi/3)} & 0 & -e^{-i(2\phi+\pi/3)} & 0 \\ 0 & 1 & 0 & -e^{-i(\phi-\pi/3)} & 0 & -e^{-i(2\phi+\pi/3)} \\ 1 & 0 & -e^{-i(\phi+\pi/3)} & 0 & -e^{-i(2\phi-\pi/3)} & 0 \\ 0 & 1 & 0 & -e^{-i(\phi+\pi/3)} & 0 & -e^{-i(2\phi-\pi/3)} \end{bmatrix}, \tag{A2}$$

where $\phi = k_x a$.

As just said, in this basis the transfer matrix, Eq. (16),

becomes block diagonal with three 2×2 matrices in its diagonal. The three pairs of modes, h, $l+$ and $l-$, decouple and propagate independently. If we put ourselves around the Dirac point $\mathbf{K}_+ = (0,-1)\nu 4\pi/(3\sqrt{3}a)$, the upper matrix corresponds to the high-energy mode, the middle one corresponds to the Dirac cone identified by $\nu=-1$, while the lower matrix stands for the cone identified by $\nu=+1$. For a general energy and momentum these three matrices read

$$\mathbb{T}_h(\epsilon,\phi) = \frac{1}{1+e^{i\phi}}\begin{bmatrix} -1 & -\epsilon \\ \epsilon & \epsilon^2-2-2\cos\phi \end{bmatrix}, \quad \text{(A3a)}$$

$$\mathbb{T}_{l-}(\epsilon,\phi) = f(\phi)\begin{bmatrix} -1 & -\epsilon \\ \epsilon & \epsilon^2+\frac{e^{-i(\phi-\frac{\pi}{3})}-1}{f(\phi)} \end{bmatrix}, \quad \text{(A3b)}$$

$$\mathbb{T}_{l+}(\epsilon,\phi) = g(\phi)\begin{bmatrix} -1 & -\epsilon \\ \epsilon & \epsilon^2+\frac{e^{-i(\phi+\frac{\pi}{3})}-1}{g(\phi)} \end{bmatrix}, \quad \text{(A3c)}$$

where we have again used $\phi = k_x a$ and have defined $f(\phi)$ and $g(\phi)$ as

$$f(\phi) = \frac{e^{i\pi/3}-e^{-i\phi}}{1-2\cos\phi}, \quad \text{(A4a)}$$

$$g(\phi) = \frac{e^{-i\pi/3}-e^{-i\phi}}{1-2\cos\phi}. \quad \text{(A4b)}$$

Appendix B: The boundary condition of the 7557 and t7t5 grain boundaries

In this appendix we will briefly compute the boundary condition matrix associated with the two grain boundaries investigated in Section VI.

1. The boundary condition of the 7557 grain boundary

Let us start by computing the boundary condition matrix relating the wave-function amplitudes on either side of the 7557 grain boundary (see Fig. 12 for a scheme of its crystalline structure). The tight-binding equations at the defect region read

$$-\frac{\epsilon}{t}\mathbf{B}(0) = \mathbf{A}(1) + \mathcal{X}^T\mathbf{D} + \mathcal{B}\mathbf{A}(0), \quad \text{(B1a)}$$

$$-\frac{\epsilon}{t}\mathbf{D} = \mathcal{X}\big(\mathbf{A}(0)+\mathbf{B}(0)\big) + \mathcal{G}\mathbf{D}, \quad \text{(B1b)}$$

$$-\frac{\epsilon}{t}\mathbf{A}(0) = \mathcal{X}^T\mathbf{D} + W_A^\dagger\mathbf{B}(-1) + \mathcal{B}\mathbf{B}(0), \quad \text{(B1c)}$$

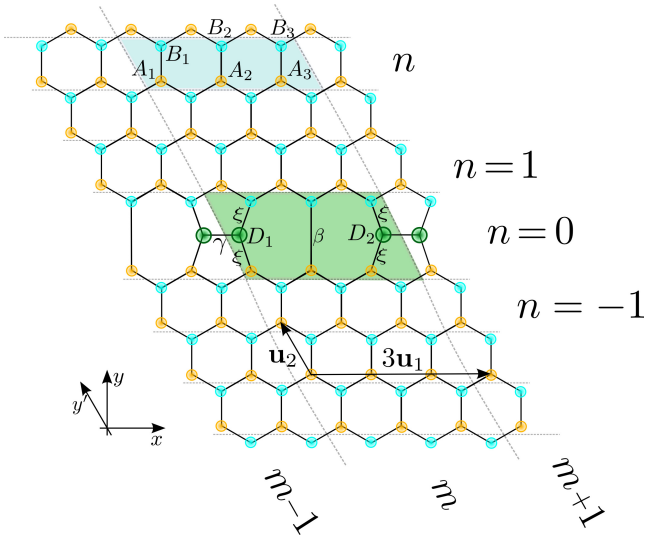

FIG. 12. Crystalline structure of the 7557 grain boundary.[33] The region of the defect line is highlighted in blue.

where we use the notation $\mathbf{Z}(n) = [Z_1(n), Z_2(n), Z_3(n)]^T$ with $Z = A, B, D$. The matrices $\mathcal{X}$, $\mathcal{B}$ and $\mathcal{G}$ read

$$\mathcal{X} = \begin{bmatrix} \xi & 0 & 0 \\ 0 & 0 & \xi \\ 0 & 0 & 0 \end{bmatrix}, \quad \text{(B2a)}$$

$$\mathcal{B} = \begin{bmatrix} 0 & 0 & 0 \\ 0 & \beta & 0 \\ 0 & 0 & 0 \end{bmatrix}, \quad \text{(B2b)}$$

$$\mathcal{G} = \begin{bmatrix} 0 & \gamma e^{-i3\phi} & 0 \\ \gamma e^{i3\phi} & 0 & 0 \\ 0 & 0 & 0 \end{bmatrix}, \quad \text{(B2c)}$$

where $\phi = k_x a$.

The above equations give the boundary condition between either side of the grain boundary which reads

$$\begin{bmatrix} \mathbf{B}(1) \\ \mathbf{A}(1) \end{bmatrix} = \mathbb{M}_1.\mathbb{M}_2 \begin{bmatrix} \mathbf{B}(-1) \\ \mathbf{A}(-1) \end{bmatrix}, \quad \text{(B3)}$$

where the $\mathbb{N}_i$ are 6×6 matrices that read

$$\mathbb{M}_1 = \begin{bmatrix} \frac{\epsilon}{t}\mathcal{P} - W_A^\dagger & \frac{\epsilon}{t}\mathcal{Q} \\ -\mathcal{P} & -\mathcal{Q} \end{bmatrix}, \quad \text{(B4a)}$$

$$\mathbb{M}_2 = \begin{bmatrix} \mathcal{Q}^{-1}\big(\frac{\epsilon}{t}\mathcal{P}W_A^{-1} - W_A^\dagger\big) & \mathcal{Q}^{-1}\mathcal{P}W_A^{-1} \\ -\frac{\epsilon}{t}W_A^{-1} & -W_A^{-1} \end{bmatrix}. \quad \text{(B4b)}$$

In Eqs. (B4) we have used the following definitions for the matrices $\mathcal{P}$ and $\mathcal{Q}$,

$$\mathcal{P} = \frac{\epsilon}{t}\mathbb{I}_3 - \mathcal{X}^T\mathcal{R}, \quad \text{(B5a)}$$

$$\mathcal{Q} = \mathcal{B} + \mathcal{X}^T\mathcal{R}, \quad \text{(B5b)}$$

where $\mathbb{I}_3$ stands for the 3×3 identity matrix, while the matrix $\mathcal{R}$ reads

$$\mathcal{R} = -\frac{1}{\xi^2}\begin{bmatrix} \epsilon & 0 & e^{-3i\phi}\gamma \\ 0 & -\frac{\xi^2}{\beta} & 0 \\ e^{3i\phi}\gamma & 0 & \epsilon \end{bmatrix}. \quad \text{(B6)}$$

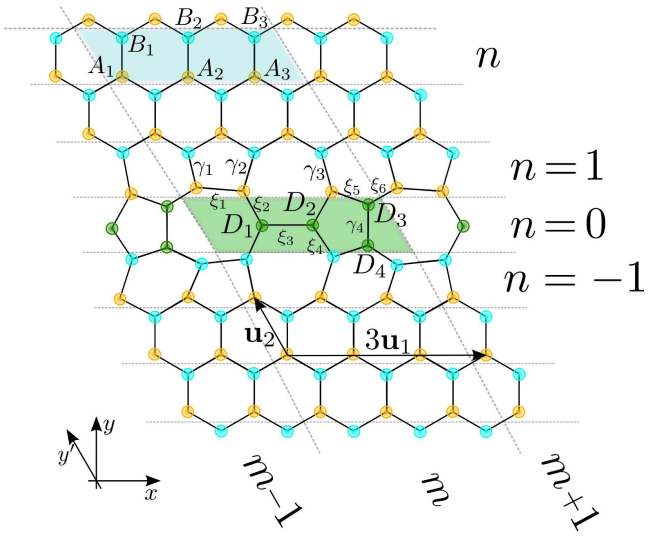

FIG. 13. Crystalline structure of the t7t5 defect line.[32] The region of the defect line is highlighted in blue.

Note that the above matrices depend on the reduced energy, ϵ/t, the longitudinal momentum, k_x, and the hopping parameters at the defect, ξ, γ and β. Similarly, the boundary condition connecting the two sides of the defect, i. e., $\mathbf{L}(1) = \mathbb{M}_{7557}.\mathbf{L}(-1)$, reads

$$\mathbb{M}_{7557} = R.\mathbb{M}_1.\mathbb{M}_2.R^T, \tag{B7}$$

and in general depends on ξ, γ, β, ϵ/t and k_x.

2. The boundary condition of the t7t5 grain boundary

In Fig. 13 we can see the scheme of the crystalline structure of a t7t5 grain boundary. In what follows we will compute the boundary condition matrix relating the wave-function amplitudes on either of its sides. For such a grain boundary, the tight-binding equations in the defect region read

$$-\frac{\epsilon}{t}\mathbf{B}(1) = G_+\mathbf{A}(1) + W_A\mathbf{A}(2), \tag{B8a}$$
$$-\frac{\epsilon}{t}\mathbf{A}(1) = G_+\mathbf{B}(1) + X_1\mathbf{A}(1) + X_2\mathbf{D}, \tag{B8b}$$
$$-\frac{\epsilon}{t}\mathbf{D} = X_2^\dagger\mathbf{A}(1) + \mathcal{S}\mathbf{D} + X_3\mathbf{B}(-1), \tag{B8c}$$
$$-\frac{\epsilon}{t}\mathbf{B}(-1) = G_-\mathbf{A}(-1) + X_3^{\mathrm{T}}\mathbf{D} + X_4\mathbf{B}(-1), \tag{B8d}$$
$$-\frac{\epsilon}{t}\mathbf{A}(-1) = G_-\mathbf{B}(-1) + W_A^\dagger\mathbf{B}(-2), \tag{B8e}$$

where, once more we use the notation $\mathbf{Z}(n) = [Z_1(n), Z_2(n), Z_3(n)]^T$, now for $Z = A, B, D$. The $G_\pm$ are diagonal matrices that can be written as $G_+ = \mathrm{diag}[\gamma_1, \gamma_2, \gamma_3]$ and $G_- = \mathrm{diag}[\gamma_2, \gamma_3, \gamma_1]$, while the X_i matrices (with $i = 1, 2, 3, 4$) read

$$X_1 = \xi_1 \begin{bmatrix} 0 & 1 & 0 \\ 1 & 0 & 0 \\ 0 & 0 & 0 \end{bmatrix}, \tag{B9}$$
$$X_2 = \begin{bmatrix} 0 & 0 & \xi_6 e^{-i3\phi} & 0 \\ \xi_2 & 0 & 0 & 0 \\ 0 & \xi_4 & \xi_5 & 0 \end{bmatrix}, \tag{B10}$$
$$X_3 = \begin{bmatrix} \xi_2 & 0 & 0 \\ 0 & \xi_4 & 0 \\ 0 & 0 & 0 \\ 0 & \xi_5 & \xi_6 \end{bmatrix}, \tag{B11}$$
$$X_4 = \xi_1 \begin{bmatrix} 0 & 0 & e^{-i3\phi} \\ 0 & 0 & 0 \\ e^{i3\phi} & 0 & 0 \end{bmatrix}, \tag{B12}$$

where again $\phi = k_x a$. Finally, $\mathcal{S}$ reads

$$\mathcal{S} = \begin{bmatrix} 0 & \xi_3 & 0 & 0 \\ \xi_3 & 0 & 0 & 0 \\ 0 & 0 & 0 & \xi_4 \\ 0 & 0 & \xi_4 & 0 \end{bmatrix}. \tag{B13}$$

We can rewrite the above equations in a more compact form that allows us to write the equation relating the amplitudes at each side of the grain boundary (i. e., those at $n = 2$ with those at $n = -2$) in the following way

$$\begin{bmatrix} \mathbf{B}(2) \\ \mathbf{A}(2) \end{bmatrix} = \mathbb{N}_1.\mathbb{N}_2.\mathbb{N}_3.\mathbb{N}_4.\mathbb{N}_5.\mathbb{N}_6 \begin{bmatrix} \mathbf{B}(-2) \\ \mathbf{A}(-2) \end{bmatrix}, \tag{B14}$$

where the matrices $\mathbb{N}_i$ are now 6×6 reading

$$\mathbb{N}_1 = -\begin{bmatrix} \frac{\epsilon}{t}\mathbb{I}_3 & (W_A)^\dagger \\ -\mathbb{I}_3 & 0 \end{bmatrix}, \tag{B15a}$$
$$\mathbb{N}_2 = -\begin{bmatrix} \frac{\epsilon}{t}(W_A)^{-1} & (W_A)^{-1}G_+ \\ -\mathbb{I}_3 & 0 \end{bmatrix}, \tag{B15b}$$
$$\mathbb{N}_3 = -\begin{bmatrix} G_+^{-1}F_1 & G_+^{-1}X_2P^{-1}X_3 \\ -\mathbb{I}_3 & 0 \end{bmatrix}, \tag{B15c}$$

and

$$\mathbb{N}_4 = -\begin{bmatrix} Q^{-1}F_2 & Q^{-1}G_-^{-1} \\ -\mathbb{I}_3 & 0 \end{bmatrix}, \tag{B15d}$$
$$\mathbb{N}_5 = -\begin{bmatrix} \frac{\epsilon}{t}G_-^{-1} & G_-^{-1}(W_A)^\dagger \\ -\mathbb{I}_3 & 0 \end{bmatrix}, \tag{B15e}$$
$$\mathbb{N}_6 = -\begin{bmatrix} \frac{\epsilon}{t}W_A^{-1} & W_A^{-1} \\ -\mathbb{I}_3 & 0 \end{bmatrix}, \tag{B15f}$$

where we have used the following definitions

$$F_1 = \frac{\epsilon}{t}\mathbb{I}_3 + X_1 + X_2P^{-1}X_2^\dagger, \tag{B16a}$$
$$F_2 = \frac{\epsilon}{t}\mathbb{I}_3 + X_3^{\mathrm{T}}P^{-1}X_3 + X_4, \tag{B16b}$$
$$P = -\frac{\epsilon}{t}\mathbb{I}_3 - \mathcal{S}, \tag{B16c}$$
$$Q = X_3^{\mathrm{T}}P^{-1}X_2^\dagger, \tag{B16d}$$

The above matrices depend on the reduced energy, ϵ/t, the longitudinal momentum, k_x, and the hopping parameters at the defect, ξ_i and γ_j (with $i = 1, \ldots, 6$ and $j = 1, \ldots, 4$).

It is now straightforward to write the boundary condition connecting the two sides of the defect $\mathbf{L}(1) = \mathbb{M}_{t7t5}.\mathbf{L}(-1)$, where the boundary condition matrix, $\mathbb{M}$, is a 6×6 matrix given by

$$\mathbb{M}_{t7t5} = R.\mathbb{N}_1.\mathbb{N}_2.\mathbb{N}_3.\mathbb{N}_4.\mathbb{N}_5.\mathbb{N}_6.R^T, \qquad \text{(B17)}$$

where, for the sake of simplicity of notation, we have omitted the dependence of the matrices $\mathbb{M}_{t7t5}$ and $\mathbb{N}_i$ on ϵ/t, k_x, ξ_i and γ_j.

---

* Corresponding author: carlos.gonzalez@fca.unicamp.br

[1] X. Li, W. Cai, J. An, S. Kim, J. Nah, D. Yang, R. Piner, A. Velamakanni, I. Jung, E. Tutuc, S. K. Banerjee, L. Colombo, and R. S. Ruoff, Science **324**, 1312 (2009).

[2] A. Reina, X. Jia, J. Ho, D. Nezich, H. Son, V. Bulovic, M. S. Dresselhaus, and J. Kong, Nano Letters **9**, 30 (2009).

[3] K. S. Kim, Y. Zhao, H. Jang, S. Y. Lee, J. M. Kim, K. S. Kim, J.-H. Ahn, P. Kim, J.-Y. Choi, and B. H. Hong, Nature **457**, 706 (2009).

[4] S. Bae, H. Kim, Y. Lee, X. Xu, J.-S. Park, Y. Zheng, J. Balakrishnan, T. Lei, H. Ri Kim, Y. I. Song, Y.-J. Kim, K. S. Kim, B. Ozyilmaz, J.-H. Ahn, B. H. Hong, and S. Iijima, Nature Nanotechnology **5**, 574 (2010).

[5] J. C. Meyer, C. Kisielowski, R. Erni, M. D. Rossell, M. F. Crommie, and A. Zettl, Nano Letters **8**, 3582 (2008).

[6] J. Lahiri, Y. Lin, P. Bozkurt, I. I. Oleynik, and M. Batzill, Nature Nanotechnology **5**, 326 (2010).

[7] Huang Pinshane Y., Ruiz-Vargas Carlos S., van der Zande Arend M., Whitney William S., Levendorf Mark P., Kevek Joshua W., Garg Shivank, Alden Jonathan S., Hustedt Caleb J., Zhu Ye, Park Jiwoong, McEuen Paul L., and Muller David A., Nature **469**, 389 (2011).

[8] K. Kim, Z. Lee, W. Regan, C. Kisielowski, M. F. Crommie, and A. Zettl, ACS Nano **5**, 2142 (2011).

[9] P. Nemes-Incze, K. J. Yoo, L. Tapaszto, G. Dobrik, J. Labar, Z. E. Horvath, C. Hwang, and L. P. Biro, Appl. Phys. Lett. **99**, 023104 (2011).

[10] P. Avouris and C. Dimitrakopoulos, Materials Today **15**, 86 (2012).

[11] Fiori Gianluca, Bonaccorso Francesco, Iannaccone Giuseppe, Palacios Tomas, Neumaier Daniel, Seabaugh Alan, Banerjee Sanjay K., and Colombo Luigi, Nat Nano **9**, 768 (2014).

[12] A. W. Tsen, L. Brown, M. P. Levendorf, F. Ghahari, P. Y. Huang, R. W. Havener, C. S. Ruiz-Vargas, D. A. Muller, P. Kim, and J. Park, Science **336**, 1143 (2012).

[13] B. Yang, H. Xu, J. Lu, and K. P. Loh, Journal of the American Chemical Society **136**, 12041 (2014).

[14] Y. Tison, J. Lagoute, V. Repain, C. Chacon, Y. Girard, F. Joucken, R. Sporken, F. Gargiulo, O. V. Yazyev, and S. Rousset, Nano Letters **14**, 6382 (2014).

[15] Y. O. V. and C. Y. P., Nat Nano **9**, 755 (2014).

[16] D. Gunlycke and C. T. White, Phys. Rev. Lett. **106**, 136806 (2011).

[17] A. Ayuela, W. Jasklski, H. Santos, and L. Chico, New Journal of Physics **16**, 083018 (2014).

[18] J. N. B. Rodrigues, N. M. R. Peres, and J. M. B. L. dos Santos, Journal of Physics: Condensed Matter **25**, 075303 (2013).

[19] J. N. B. Rodrigues, N. M. R. Peres, and J. M. B. Lopes dos Santos, Phys. Rev. B **86**, 214206 (2012).

[20] D. Gunlycke and C. T. White, Phys. Rev. B **90**, 035452 (2014).

[21] J.-H. Chen, G. Autès, N. Alem, F. Gargiulo, A. Gautam, M. Linck, C. Kisielowski, O. V. Yazyev, S. G. Louie, and A. Zettl, Phys. Rev. B **89**, 121407 (2014).

[22] S. Malola, H. Häkkinen, and P. Koskinen, Phys. Rev. B **81**, 165447 (2010).

[23] Y. Liu and B. I. Yakobson, Nano Lett. **10**, 2178 (2010).

[24] O. V. Yazyev and S. G. Louie, Phys. Rev. B **81**, 195420 (2010).

[25] O. V. Yazyev and S. G. Louie, Nature Materials **9**, 806 (2010).

[26] R. Grantab, V. B. Shenoy, and R. S. Ruoff, Science **330**, 946 (2011).

[27] L. Jiang, X. Lv, and Y. Zheng, Physics Letters A **376**, 136 (2011).

[28] J. Liwei, Y. Guodong, G. Wenzhu, L. Zhe, and Z. Yisong, Phys. Rev. B **86**, 165433 (2012).

[29] Q. Yu, L. A. Jauregui, W. Wu, R. Colby, J. Tian, Z. Su, H. Cao, Z. Liu, D. Pandey, D. Wei, T. F. Chung, P. Peng, N. P. Guisinger, E. A. Stach, J. Bao, S.-S. Pei, and Y. P. Chen, Nature Materials **10**, 443 (2011).

[30] L. A. Jauregui, H. Cao, W. Wu, Q. Yu, and Y. P. Chen, Solid State Communications **151**, 1100 (2011).

[31] J. González, H. Santos, M. Pacheco, L. Chico, and L. Brey, Phys. Rev. B **81**, 195406 (2010).

[32] A. R. Botello-Mendez, X. Declerck, M. Terrones, H. Terrones, and J.-C. Charlier, Nanoscale **3**, 2868 (2011).

[33] N. Ansari, F. Nazari, and F. Illas, Phys. Chem. Chem. Phys. **16**, 21473 (2014).

[34] A. B. Kuzmenko, I. Crassee, D. van der Marel, P. Blake, and K. S. Novoselov, Phys. Rev. B **80**, 165406 (2009).

[35] S. Datta, *Electronic Transport in Mesoscopic Systems* (CUP, Cambridge, 1999).

[36] M. P. L. Sancho, J. M. L. Sancho, J. M. L. Sancho, and J. Rubio, Journal of Physics F: Metal Physics **15**, 851 (1985).

[37] A.-P. J. H. Haug, *Quantum Kinetics in Transport and Optics of Semiconductors* (Springer Berlin Heidelberg, 2008).

[38] J. Wilhelm, M. Walz, and F. Evers, Phys. Rev. B **89**, 195406 (2014).

[39] P. Vancs, G. I. Mrk, P. Lambin, A. Mayer, C. Hwang, and L. P. Bir, Applied Surface Science **291**, 58 (2014), e-MRS 2013 Spring Meeting , Symposium I: The route to post-Si {CMOS} devices: from high mobility channels to graphene-like 2D nanosheets.

[40] P. Vancs, G. I. Mrk, P. Lambin, A. Mayer, Y.-S. Kim, C. Hwang, and L. P. Bir, Carbon **64**, 101 (2013).

[41] D. A. Bahamon, A. L. C. Pereira, and P. A. Schulz, Phys. Rev. B **83**, 155436 (2011).

[42] E. V. Castro, K. S. Novoselov, S. V. Morozov, N. M. R. Peres, J. M. B. L. dos Santos, J. Nilsson, F. Guinea, A. K. Geim, and A. H. C. Neto, Journal of Physics: Condensed

Matter **22**, 175503 (2010).
[43] C. J. Páez, D. A. Bahamon, and A. L. C. Pereira, Phys. Rev. B **90**, 125426 (2014).
[44] E. McCann, Phys. Rev. B **74**, 161403 (2006).
[45] M. Koshino and T. Ando, Phys. Rev. B **73**, 245403 (2006).
[46] M. S. Tang, C. Z. Wang, C. T. Chan, and K. M. Ho, Phys. Rev. B **53**, 979 (1996).